

HOW UNIFORM IS TEV-BLAZAR HEATING?

ASTRID LAMBERTS¹, PHILIP CHANG¹, EWALD PUCHWEIN², CHRISTOPH PFROMMER³, AVERY E. BRODERICK^{4,5} AND MOHAMAD SHALABY^{2,3,6}

¹ Department of Physics, University of Wisconsin-Milwaukee, 1900 East Kenwood lowBoulevard, Milwaukee WI 53211, USA

² Institute of Astronomy and Kavli Institute for Cosmology, University of Cambridge, Madingley Road, Cambridge, CB3 0HA, UK

³ Heidelberg Institute for Theoretical Studies, Schloss-Wolfsbrunnenweg 35, D-69118 Heidelberg, Germany

⁴ Perimeter Institute for Theoretical Physics, 31 Caroline Street North, Waterloo, ON, N2L 2Y5, Canada

⁵ Department of Physics and Astronomy, University of Waterloo, 200 University Avenue West, Waterloo, ON, N2L 3G1, Canada and

⁶ Department of Physics, Faculty of Science, Cairo University, Giza 12613, Egypt

Draft version October 16, 2014

ABSTRACT

TeV-blazars **likely** heat the intergalactic medium (IGM) as their gamma rays interact with photons of the extragalactic background light to produce electron-positron pairs, which lose their kinetic energy to the surrounding medium through plasma instabilities. Assuming uniform heating, this mechanism increases the temperature of the IGM and produces an inverted temperature-density relation in underdense regions. This additional heating source significantly impacts large scale structure formation. In this paper we go beyond the approximation of uniform heating and quantify the heating rate fluctuations and their impact on the thermal history of the IGM. We analytically compute a filtering function that relates the heating rate fluctuations to the underlying dark matter density field. We implement it in the cosmological code GADGET-3 and perform large scale simulations to determine the impact of inhomogeneous heating. We show that, because of the bias, blazar heating is inhomogeneous, at all redshifts. The temperature-density relation shows an important scatter and presents a low temperature envelope of unheated regions, **in particular at low densities and within voids**. However, the median temperature of the IGM is close to that in the uniform case, albeit slightly lower at low redshift. We find that blazar heating is more complex than initially assumed and that the temperature-density relation is not unique. **Future work will deal with the observational impact and large scale structure formation in this context.** Our analytic model for the heating rate fluctuations couples well with large scale simulations and provides a cost-effective alternative to subgrid models.

Subject headings: BL Lacertae objects: general, cosmology: theory, gamma-rays: general, intergalactic medium, large-scale structure of universe

1. INTRODUCTION

The intergalactic medium is an ionized medium in which galaxies and clusters are embedded, thus forming the cosmic web (Bond et al. 1996). It constitutes the main reservoir of baryons available for the formation of collapsed objects such as galaxies and clusters (Rauch et al. 1997). The intergalactic medium constitutes the bulk of the baryons forming the cosmic web (Bond et al. 1996) as well as the reservoir of baryons available for the formation of galaxies and clusters (Rauch et al. 1997). Observations of metal-enriched gas (see e.g. Simionescu et al. (2009); Werner et al. (2010)) prove link its evolution due to already formed stars and galaxies to the formation of galaxies and stars. This close relation between the IGM and structure evolution the objects that are embedded in it makes it a crucial aspect of understanding large-scale structure formation in the universe. The temperature of the IGM is mostly set by photoionization of hydrogen and helium, competing with adiabatic cooling. **As a result, the universe is slowly cooling once reionization is completed. The IGM temperature is expected to increase with density because denser regions experience a lower amount of adiabatic**

cooling, as well as more recombination-induced photoheating. Gas in the IGM that has not been shock heated provides a lower envelope to the temperature density relation distribution. This yields a slowly cooling universe, with denser regions being warmer because more resistant to adiabatic cooling. Observations of Lyman α absorption lines in the spectra of background quasars due to neutral gas confirm the positive slope of the temperature-density relation this equation-of-state (Schaye et al. 2000; Ricotti et al. 2000; Rudie et al. 2012) with only a temporary flattening around $z \sim 3$. The latter is expected due to He II reionization (e.g. McQuinn et al. 2009; Compostella et al. 2013; Puchwein et al. 2014). However, recent measurements found that underdense regions may be warmer than expected predicted (Viel et al. 2009; Bolton et al. 2008), as well as unexpectedly high temperatures at $z < 2$ (Boera et al. 2014). Although an inverted temperature-density relation in underdense regions has not been firmly established yet (Bolton et al. 2014), these observations suggest the thermal history of the IGM may be more complex than initially assumed. Broderick et al. (2012) recently discovered a complementary heating mechanism, through TeV blazars. TeV blazars are active galactic nuclei (AGN) emitting very high energy gamma rays ($E \geq 100$ GeV). They belong to the radio-loud sub-

group of AGN, with the relativistic jet being pointed towards us. About 50 of these sources have been significantly discovered so far (<http://tevcat.uchicago.edu/>) by the ground based Cerenkov telescopes such as MAGIC, H.E.S.S. and VERITAS. Those pointed observations have only skimmed the surface of a much larger population that manifest themselves as hard-spectra gamma-ray blazars as observed with the space-based *Fermi*/LAT telescope (Broderick et al. 2014). The universe is mainly opaque to very high energy gamma rays, as they interact with the extragalactic background light (EBL) producing electron/positron pairs (Gould & Schréder 1967; Stecker et al. 1992). It is commonly assumed that the electron/positron pairs scatter photons of the cosmic microwave background up in energy, resulting in a distribution of photons with energies between 0.1 and 100 GeV. Such an emission component towards TeV blazars has not been observed so far (Aleksić et al. 2010; H. E. S. S. Collaboration et al. 2014). One putative solution would be pair deflection due to the intergalactic magnetic field, thus lowering the surface brightness of the formed pair halo at GeV energies (Durrer & Neronov 2013; Vovk et al. 2012; Dermer et al. 2011). However, the cascaded GeV emission would still contribute to the extragalactic gamma-ray background (EGRB). *Fermi*/LAT was able to resolve more sources, thereby limiting the isotropic component of the unresolved EGRB and severely limiting the redshift evolution of hard blazars in this picture (REFERENCE). Carefully modeling the selection function of blazars, there appears to be no evidence for a significantly different evolution of blazars in comparison to their radio-loud analogues such as radio galaxies (Giommi et al. 2012, 2013). This provides circumstantial evidence that pair beams instead transfer their energy directly to the IGM through plasma instabilities (Broderick et al. 2012; Schlickeiser et al. 2012, 2013; Chang et al. 2015). This naturally explains the EGRB with a blazar population that exhibits a redshift evolution in agreement with that of quasars (Broderick et al. 2014, 2013). The pairs constitute a dilute, ultrarelativistic beam, which is subject to several plasma instabilities, from which the “oblique” instability (Bret et al. 2004) is the most powerful. Assuming its efficiency in the linear regime extends to the non-linear regime, Chang et al. (2012) show it is responsible for increasing the temperature of the IGM by almost a factor 10 in low density regions. While this assumption is still debated (see Miniati & Elyiv (2013); Sironi & Giannios (2014) but also Schlickeiser et al. (2013, 2012); Chang et al. (2015)), throughout all this paper we will assume plasma instabilities are the dominant mechanism for cooling of the pair beams. Including TeV blazar heating in the thermal history of the IGM, Chang et al. (2012) were able to reproduce the inverted temperature-density relation for low density regions. In a follow-up paper, Pfrommer et al. (2012) found that TeV blazar heating is responsible for creating a redshift dependent entropy floor in clusters and galaxies, thus suppressing the formation of dwarf galaxies after the peak of blazar activity at redshift $z \simeq 2$ and potentially providing an explanation to the “missing

satellite problem” (Kravtsov 2010). Implementing volumetric, i.e. uniform, uniform blazar heating, i.e. with a redshift-dependent but spatially homogeneous energy deposition rate per unit volume, in a cosmological hydrodynamical simulation of galaxy formation, Puchwein et al. (2012) find excellent agreement with the one and two-point statistics of the Ly α forest, which is the main observational tracer of low density regions in the universe. However, the low thermal broadening of certain Lyman α lines indicates the presence of cold gas (Rudie et al. 2012), which suggests TeV blazar heating does not uniformly heat the whole universe. It is natural to expect a larger TeV flux close to higher density regions where visible structures form. Conversely, in large underdense regions, far from massive black holes, heating is probably much lower. The goal of this paper is to go beyond the hypothesis of uniform heating and to link TeV blazar heating to the underlying clustered density field and take into account the bias of sources. This will lead to a more heterogeneous heating pattern and account for unheated regions while keeping the overall impact of blazar heating. Self-consistently studying the evolution of the IGM from first principles involves modeling both the formation and evolution of galaxies at the largest scales of the universe. As this is still far beyond reach of current computers, we have determined a filter function which relates the heating fluctuations to the dark matter structure similarly to Pritchard & Furlanetto (2007); Barkana & Loeb (2005); Pontzen (2014). Based on the hierarchical structure formation in a Λ CDM universe, it naturally selects the relevant length scales for TeV blazar heating (§2). We have implemented it in large scale cosmological simulations (§3) in order to focus on the equation of state and thermal evolution of the IGM (§4). We then discuss how inhomogeneous heating could reconcile different observations (§5) and conclude (§6).

2. DETERMINING THE WINDOW FUNCTION

2.1. Intuitive understanding

One zone models (Chang et al. 2012; Pfrommer et al. 2012) and numerical simulations (Puchwein et al. 2012) of blazar heating on the IGM assume that the heating is uniform. Because the heating rate depends on the local density of EBL and TeV photons, the assumption of uniform heating implies that the distributions of EBL and TeV photons are uniform. For EBL photons, this is likely the case, as the mean free path is larger than the Hubble length. However, for TeV photons the mean free path compares with the separation between TeV sources for $z \geq 1$, so the spatial fluctuations in the heating rate are likely nontrivial. Moreover, the sources of TeV photons tend to be clustered and so the IGM near these clustered regions will get an increased flux of photons in comparison to low-density regions because of the increased number of sources and the $1/r^2$ flux dilution with increasing distance r from the source. Our goal is to include a more realistic model for heating due to TeV blazars in numerical simulations. To properly calculate the heating fluctuations due to TeV blazar heating, the formation and evolution of accreting supermassive black holes must be modeled in a full self-consistent cosmological simulation. In addition, the TeV

radiation from these systems must be ray-traced through the simulation volume. Such a task is computationally intractable. As a result, we have elected to model this TeV blazar heating in a more statistical manner. We assume that TeV blazars are associated with galaxies and that they roughly emit over 4π steradian. The latter assumption remains valid so long as the number of TeV blazars is large enough such that every spot in the universe is illuminated by at least a few TeV blazars, **which is the case for $z \lesssim 6$** (Chang et al. 2012). The heating rate at a given point \mathbf{x} is determined by the received TeV flux from all the sources within a certain radius r_{\max} , where r_{\max} is much larger than the mean free path of gamma rays.

$$\dot{Q}(\mathbf{x}, z) = \frac{1}{4\pi} \int_{\Omega} \int_0^{r_{\max}} \mathcal{E}(\mathbf{r}' + \mathbf{x}, z) \sigma n_{\text{EBL}}(z) e^{-\tau} dr' d\Omega, \quad (1)$$

where \dot{Q} and \mathcal{E} are the heating rate density and emissivity of the sources (both in units of energy per unit time and per unit volume), σ (in cm^{-2}) is the energy-averaged cross section for pair production on the EBL and τ is the associated optical depth along the line of sight. One can then express the resulting heating rate as a mean value \bar{Q} and a first order correction δ_H .

$$\dot{Q}(\mathbf{x}, z) = \bar{Q}(\mathbf{x}, z) [1 + \delta_H(\mathbf{x}, z)]. \quad (2)$$

The method is based on a Taylor expansion of the quantities describing the TeV sources and keeping only the first order corrections. Transforming to Fourier space yields for the fluctuation amplitude

$$\tilde{\delta}_H(k, z) = \tilde{W}_H(k, z) \tilde{\delta}(k, z), \quad (3)$$

where \tilde{W}_H is defined as the window function and maps the Fourier transform of the overdensity, $\tilde{\delta}$, to the Fourier transform of the heating fluctuations, $\tilde{\delta}_H$. This naturally yields the relevant length scale for heating rate fluctuations. **[Does δ refer to gas or DM overdensity? In Sect 3.1, you talk about a gas overdensity...]** The detailed exposition of this method, in the Newtonian limit and in an expanding universe, is given in Appendix A. In the following section, we present the general method and highlight the underlying hypotheses of our work.

2.2. Window function for TeV blazar heating

To determine the heating rate fluctuations we express the TeV emissivity in Eq. (1) as a mean value and a first order correction. The heating rate at a given point is set by the received TeV flux from all the sources within a certain radius. We assume that the pairs lose their energy to the IGM at the point where they are created. As stated in Broderick et al. (2012), this is a reasonable assumption as the plasma instability length scales are significantly smaller than the mean free path of these TeV photons. The TeV gamma rays are emitted by accreting supermassive black holes at centers of galaxies, which cluster in overdense regions. Matter is tightly coupled to the underlying dark matter, the evolution of which is straight forward to model analytically within the linear approximation. The linear approximation is valid as long

as the overdensity is small, which is true in the early universe and then breaks down at small scales as very dense structures form. Our computation takes into account the bias between baryonic matter and dark matter (Mo & White 1996), as we detail below. To model cosmic distances, Eq. (1) is integrated in redshift space and we take into account the resulting energy loss for the TeV photons as well as first order corrections due to proper motions of the sources within the Hubble flow (Kaiser 1987). We integrate over the energy distribution of the TeV-emission. We thus get

$$\begin{aligned} \tilde{W}_H(k, z) = & \frac{1}{\bar{X}} \int_{E_{\min}}^{E_{\max}} dE \int_z^{z_{\max}} \frac{dX(E, z, z')}{dz'} \\ & \times \frac{D_{\text{pp}}(z')}{D_{\text{pp}}(z)} \left((b(z) + 1)j_0(kr) - \frac{2}{3}j_2(kr) \right) dz', \end{aligned} \quad (4)$$

with

$$X(E, z', z) = \frac{e^{-\tau(z, z', E)}(1+z)^2}{H(z')\epsilon(E', z')}. \quad (5)$$

and \bar{X} its spectral average. E is the energy of the received TeV photon and, E' its initial energy and ϵ the (comoving) blazar luminosity density. b is the bias and j_0 and j_2 are spherical Bessel functions. Assuming the TeV blazar distribution follows the redshift evolution of quasars, Broderick et al. (2012) determined the blazar luminosity density in the TeV band based on a fit to Hopkins et al. (2007)

$$\begin{aligned} \epsilon(E', z) = & \epsilon(E', z=0)\Phi_B(z) \\ \simeq & \epsilon(E', z=0)\zeta\Phi_Q(z), \end{aligned} \quad (6)$$

with $\zeta = 2.1 \times 10^{-3}$ and

$$\Phi_Q[x(z)] = 10^{-0.0037x^4 + 0.085x^3 - 0.0778x^2 + 2.795x - 2.133}, \quad (7)$$

where $x = 1+z$. As TeV blazars have power-law spectra with intrinsic (i.e. redshift corrected) spectral index α , we get

$$\epsilon(E', z=0) = \epsilon(E_0, z=0) \left(\frac{E'}{E_0} \right)^{-\alpha} \equiv \epsilon_0 \left(\frac{E'}{E_0} \right)^{-\alpha}, \quad (8)$$

with $\epsilon_0 = (1.7 - 4.8) \times 10^{-36} \text{ erg s}^{-1} \text{ cm}^{-3}$ the current blazar luminosity density. Using 28 TeV blazars, Chang et al. (2012) find that $\alpha \simeq 3$ and $E_0 \simeq 1 \text{ TeV}$. Adopting typical parameters of nearby TeV blazar spectra yields $E_{\min} = 100 \text{ GeV}$, and $E_{\max} = 10 \text{ TeV}$. Assuming blazars follow a similar evolution to quasars, we use $z_{\max} = 5$ (Hopkins et al. 2007). The optical depth is set by the mean free path $D_{\text{pp}}(E', z)$ of TeV photons before they interact with an EBL photon to produce an electron-positron pair. Its redshift evolution is set by the EBL. Despite careful work that aims at constraining it, there remain uncertainties in the star formation history of the universe as well as its metallicity and dust contents (see e.g Franceschini et al. (2008); Stecker et al. (2006)). Following Chang et al. (2012) we use a prescription

$$D_{\text{pp}}(E, z) = 35 \left(\frac{E}{1 \text{ TeV}} \right)^{-1} \left(\frac{1+z}{2} \right)^{-\xi} \text{ Mpc}, \quad (9)$$

where $\xi = 4.5$ for $z < 1$ and $\xi = 0$ for $z > 1$ (Kneiske et al. 2004; Neronov & Semikoz 2009). The proper mean

free path is constant for $z \geq 1$, however, the comoving mean free path increases for increasing redshift. The fluctuations in TeV flux are related to the distribution of blazars, which is biased with respect to the distribution of dark matter halos. Luminous structures such as galaxies preferentially populate the high peaks of the dark matter density distribution. The bias of a certain structure is the ratio between its power spectrum to the power spectrum of the dark matter halos (see e.g. Cooray & Sheth (2002) for a review). It is stronger for more massive objects, such as quasars. Due to the small number of sources and TeV photon absorption, there is no observation of TeV blazar bias. An estimate can be obtained from the observations of quasar bias (Croom et al. 2005; Myers et al. 2007; Shen et al. 2007). We use a fit to an analytic model for a halo mass of $10^{13} h^{-1} M_{\odot}$ (Basilakos et al. 2008). TeV blazars may have a stronger bias, as radio-loud AGN are generally found in a more clustered environment than quasars (Mandelbaum et al. 2009; Simpson et al. 2012). To illustrate the impact of the uncertainty on the bias, we also use a model for galaxy bias, based on a halo mass of $10^{12} h^{-1} M_{\odot}$, for comparison. [Show additional figure with $b(z)$ and fitting function.] Substituting Eqs. (6) and 9 into Eq. (4) then gives the complete window function for TeV blazar heating. Fig. 1 shows the filter for $z = 1, 2$ and 4 for a model with galaxy and quasar bias. We have computed the window function using an embedded Runge-Kutta method which is able to capture the fast variation of the Bessel functions at large wave numbers while decreasing computing time at smaller wave numbers. The window function describes how density fluc-

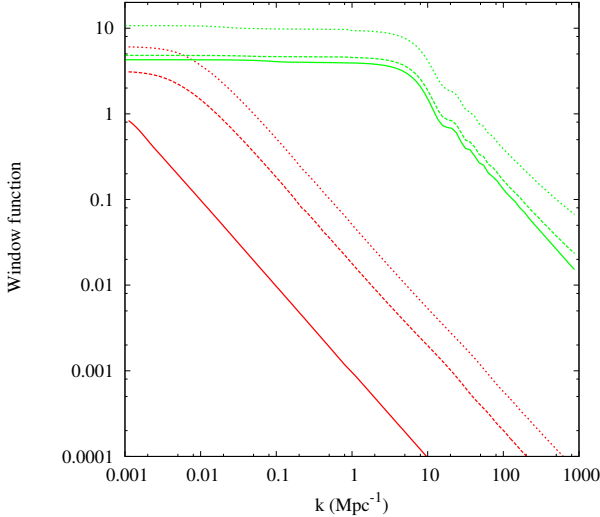


FIG. 1.— Window function for TeV blazar heating from $z = 1$ (solid lines), $z = 2$ (dashed lines) and $z = 4$ (dotted lines) for the galaxy bias model (red) and the quasar bias model (green).

tuations translate into heating fluctuations. The quasar bias model has more power at all scales because of the larger bias. Comparison with Fig. 8 (in the Appendix), computed without bias, shows that bias is responsible for values above unity in the window function. For the

galaxy model, at high redshift, most of the power resides on large scales, where blazar heating traces the density fluctuations. At smaller scales, density fluctuations have no impact and blazar heating is uniform. At the current epoch, TeV blazar heating in the galaxy bias model is close to uniform as there is power only at the largest scales (above 100 Mpc), where the Universe is essentially uniform (see Clowes et al. (2013) and references therein). For the quasar model, there is much more power at small scales and small scale density fluctuations will lead to enhanced heating. In both models, the window function remains positive at all scales, underdense regions are the only areas where a lower than average heating rate is expected. Above average heating is possible in large scale overdensities but also at smaller scales when the over-density is important. However, such regions should be analysed with caution as the linear theory for the dark matter evolution breaks down. [This is unclear: what exactly do you mean?] After these first analytic estimates, we include the window function to model TeV blazar heating in cosmological simulations.

3. NUMERICAL METHOD

3.1. Cosmological simulations

We perform simulations with the smoothed particle hydrodynamics (SPH) code GADGET-3, an upgraded version of the publicly available GADGET-2 code (Springel 2005). The code solves the gravitational evolution of both dark matter and gas particles following a TreePM N-body method. The hydrodynamical evolution of the gas is modeled using an entropy conserving scheme (Springel & Hernquist 2002). The cosmological model is based on the WMAP 7-year data (Komatsu et al. 2011): $\Omega_M = 0.272$, $\Omega_\Lambda = 0.728$, $\Omega_B = 0.0465$, $h = 0.704$ and $\sigma_8 = 0.809$. The initial conditions were evolved from $z = 100$ until $z = 1$ in boxes with comoving side length of $100 h^{-1}$ Mpc and periodic boundary conditions. We use $N = 2 \times 512^3$ particles, which gives a mass of $m_{\text{gas}} = 3.8 \times 10^6 h^{-1} M_{\odot}$ and $m_{\text{DM}} = 1.8 \times 10^7 h^{-1} M_{\odot}$ for baryonic and dark matter particles, respectively. We used a gravitational softening length of $7.8 h^{-1}$ kpc. We checked that the resolution has limited impact on the results of our simulations, performing test simulations with a comoving side length of $50 h^{-1}$ Mpc. Increasing the resolution significantly broadens the temperature distribution of the gas for $N \leq 2 \times 128$. However, there is a less than 2% difference in the median temperature and less than 8% difference in its root mean square (at $\delta = 0$) between $N = 2 \times 128$ and 2×256 , indicating numerical convergence. As we are only interested in the low density intergalactic medium, we use a simplified model for star formation which significantly speeds up the simulations. In this model, gas particles with $\delta \geq 1000$ and $T \leq 10^5$ are directly converted into stars (Viel et al. 2004). Although it results in unrealistic galaxy properties, this approximation does not affect regions with $\delta \leq 0$. Black hole feedback other than TeV blazar heating is not included. Photoheating is set by ionization equilibrium in the presence of an external UV field, which is parameterized according to Faucher-Giguère et al. (2009). As our version of the GADGET-3 code assumes ionization equilibrium when computing photoheating rates, the heating

is rather inefficient during reionization where this assumption is not well satisfied (see e.g. Puchwein et al. 2014). In this model, reionization happens too fast to allow efficient heating. Following Puchwein et al. (2012) we thus include the equivalent heat input by hand at redshift $z = 10$. The size of the box is set to model the heating perturbations on the scales determined by the window function in Fig.1. We want to model a representative cosmic sample and probe distances beyond the mean free path of the TeV photons, which is of order of 35 (comoving) Mpc at $z = 0$ (but 100 Mpc at $z = 2$). To confirm that 100 h^{-1} Mpc is a satisfactory size to model all the significant length scale, we performed a $L_{\text{box}} = 200 h^{-1}$ Mpc simulation with 512^3 particles. We compared the resulting temperature distribution function with the 100 h^{-1} Mpc box, with the same mass resolution. It differs by less than 2% for $z \geq 3$. For lower redshift, the temperature distribution is slightly wider in the larger box, but the difference remains below 10% at $z = 1$. This is consistent with studies showing that the one-and two-point statistics of the Lyman α forest are well captured with $\simeq 50 h^{-1}$ boxes (Regan et al. 2007; Bolton & Becker 2009).

3.2. Including the TeV blazar heating fluctuations

We model the impact of the fluctuations in TeV blazar heating on the thermodynamics of the IGM. For every gas particle, the blazar heating is set by the mean value plus some correction depending on the local density field (Eq. (2)). As in Puchwein et al. (2012), we adopt the mean heating rate computed by Chang et al. (2012) (Eq. (6)). We focus on the model with “intermediate” values for the blazar heating. Modeling fluctuations by implementing a filtering function in a large scale simulation is a new method. The computation of the fluctuations is done in Fourier space and is inspired by the resolution of the Poisson equation. The Fourier transforms are performed with the parallel extension of the Fast Fourier Transform Library. The first step is map the particles onto a mesh, which is done with a clouds-in-cells algorithm (Hockney & Eastwood 1981). We determine the Fourier transform of the DM density field. Then the density field is multiplied by the window function performing a bilinear interpolation of tabulated values for certain values of redshift and wavenumber. In this paper we use 21 equally spaced redshift bins from $z = 5$, where blazar heating turns on in our model, until the end of the simulation. We use 128 logarithmically equally spaced wavenumber bins. We also deconvolve for the clouds-in-cells kernel by dividing by $\text{sinc}^2(k_x L/2N)\text{sinc}^2(k_y L/2N)\text{sinc}^2(k_z L/2N)$. We then perform the inverse Fourier transform and renormalize. The last step is necessary to remap the results onto the gas particles.

4. RESULTS

Figure 2 shows the heating rate fluctuations in the mid-plane of the $L_x = 100h^{-1}$ Mpc simulation for $z = 3, 1$ for both the galaxy and quasar bias model. **Both simulation models are started from identical initial condition such that any visible difference is solely due to the different bias assumptions in the blazar heating model.** The corresponding density field is

shown in the upper column and shows increasing structure formation as the redshift decreases. The heating map has a linear scale while the density scale is logarithmic. The heating rate fluctuations are, on average, much smaller than the density fluctuations. This is because the window function filters out small scales, which correspond to collapsed regions, where density fluctuations are the highest. To the zeroth order, one can thus consider TeV blazar heating to be uniform, as was assumed in Chang et al. (2012). Additional heating (i.e. $\delta_H > 0$) occurs around clustered regions. This is expected, as the window function translates large scale density fluctuations into heating rate fluctuations. Conversely, underdense regions, such as the one around $\{x = 60, y = 70\}$ (for $z = 3$) display heating below average as they are isolated from sources, and their flux decreases as r^{-2} . As the redshift decreases, heating rate fluctuations increase, following increasing density fluctuations.

Figure 3 shows the volume weighted ratio of the full internal energy when blazar heating is included to the internal energy when blazar heating is not included as a function of the overdensity.

Figure 3 shows the ratio of the internal energy due to blazar heating with respect to the total internal energy. The color scale is logarithmic.

These maps clearly highlight that blazar heating has more impact in underdense regions, as the heating rate per baryon is higher. Even if these regions receive less heat than regions with higher density (see Fig. 2), **blazar heating can account to up to 10% of the total internal energy. blazar heating can increase the internal energy by almost two orders of magnitude at $z = 1$.** This effect increases with time, as structures grow, the dense regions get denser and the voids get less dense. **The ratio between the blazar induced energy and total energy first increases over time and then decreases between $z = 2$ and $z = 1$. This evolution is related to the blazar luminosity evolution, which peaks at $z = 2$.** The impact of inhomogeneous heating translates into a more complex temperature-density relation, as is shown on Fig. 4. The color map shows the mass weighted $T - \rho$ relation from our simulations and the grey contours show the case for uniform blazar heating with the same resolution (Puchwein et al. 2012). Temperature measures the integrated impact of TeV blazar heating over time. When clustering is taken into account, the temperature-density relation has a significant scatter for underdense regions even when we use the galaxy bias model. For the quasar bias model, this scatter results in the lower envelope of the temperature-density relation to change little from the case with no blazar heating. However, the mode of the temperature is very close to the uniform blazar heating case. At $z = 1$ the simulation with the galaxy bias model has a very similar outcome to the uniform model and blazar heating can be considered nearly homogeneous, though the lower envelope sits at a lower temperature. Figure 5 shows the mass-weighted probability distribution functions of the temperature for all the simulations. This provides a more quantitative view of the scatter in temperature. The simulation with the quasar bias model shows significant deviation from the uniform case, especially at lower redshifts. Here the ef-

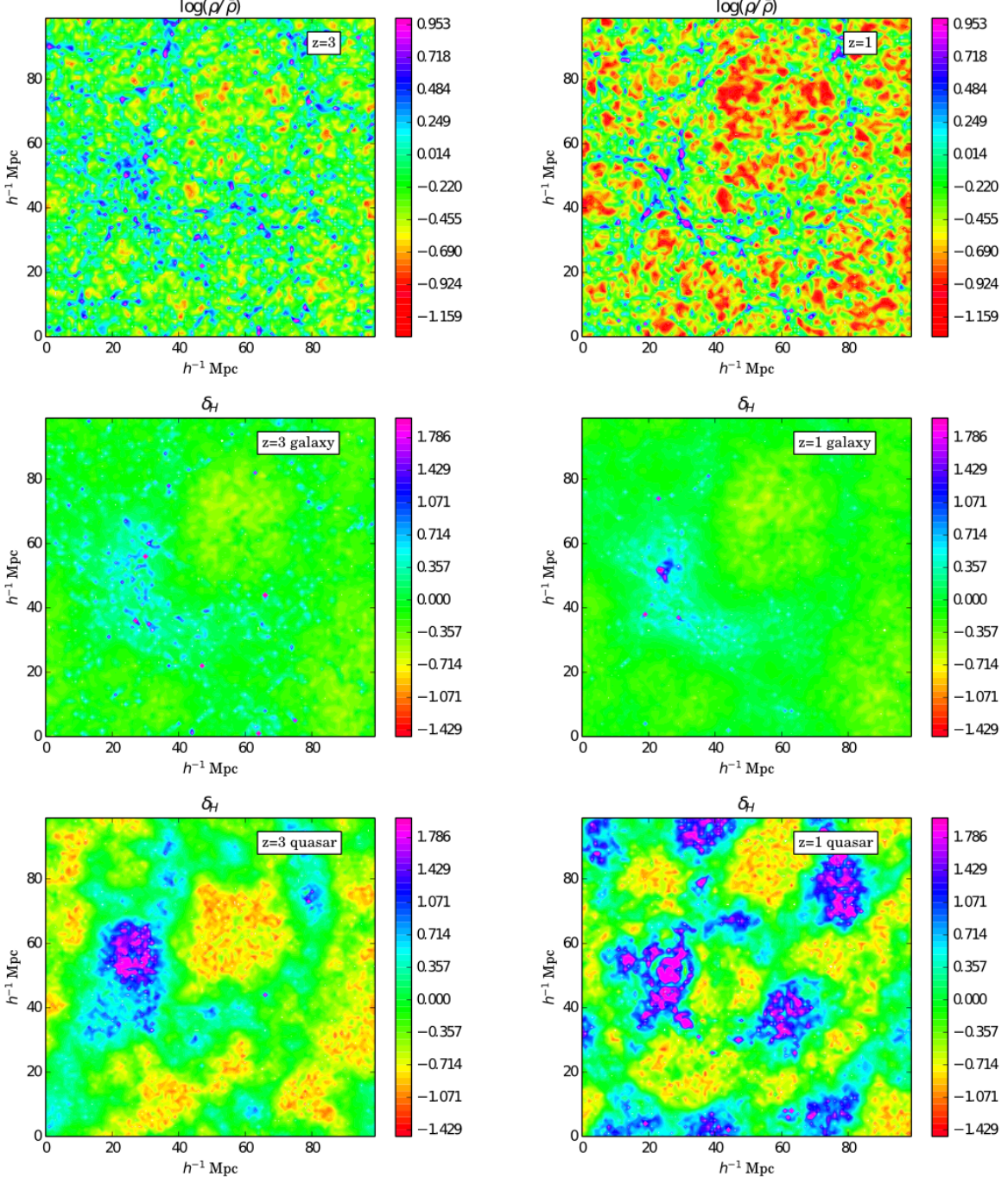


FIG. 2.— Slices through the midplane of the box, for $z = 3$ (left column) and $z = 1$ (right column) : logarithm of the density with respect to the mean value (upper row), heating rate fluctuations with the galaxy (middle row) and quasar model (lower row).

fect of the lower envelope is clear as their is a significant tail toward lower temperatures for $z \leq 3$. The scatter is strong for the quasar bias mode, where the coldest zones have $T \simeq 10^4 K$ while the warmest zones have $T \simeq 3^4 K$ for $z = 3$. Conversely, the warmest gas is only slightly warmer than the mode of the temperature. The probability distribution function clearly highlights the impact of clustering on TeV blazar heating. To have a better understanding of the heating fluctuations with respect to density fluctuations we represent the mass-weighted $\delta_H - \delta$ distribution on Fig. 6. The heating rate represents an instantaneous view of the impact of TeV blazar

heating. In the quasar bias model (**lower row**), most of the particles receive slightly more heat than in the uniform case. However, the additional heat is only a few times more than the uniform case. On the contrary, certain regions receive orders of magnitude less heat than the mean value. These areas suffer from the decrease of the TeV flux and isolation from massive structures. This is consistent with the temperature probability distribution function presenting an important low temperature tail and a low probability for high temperatures. In the galaxy model, most of the gas is heated similarly to the

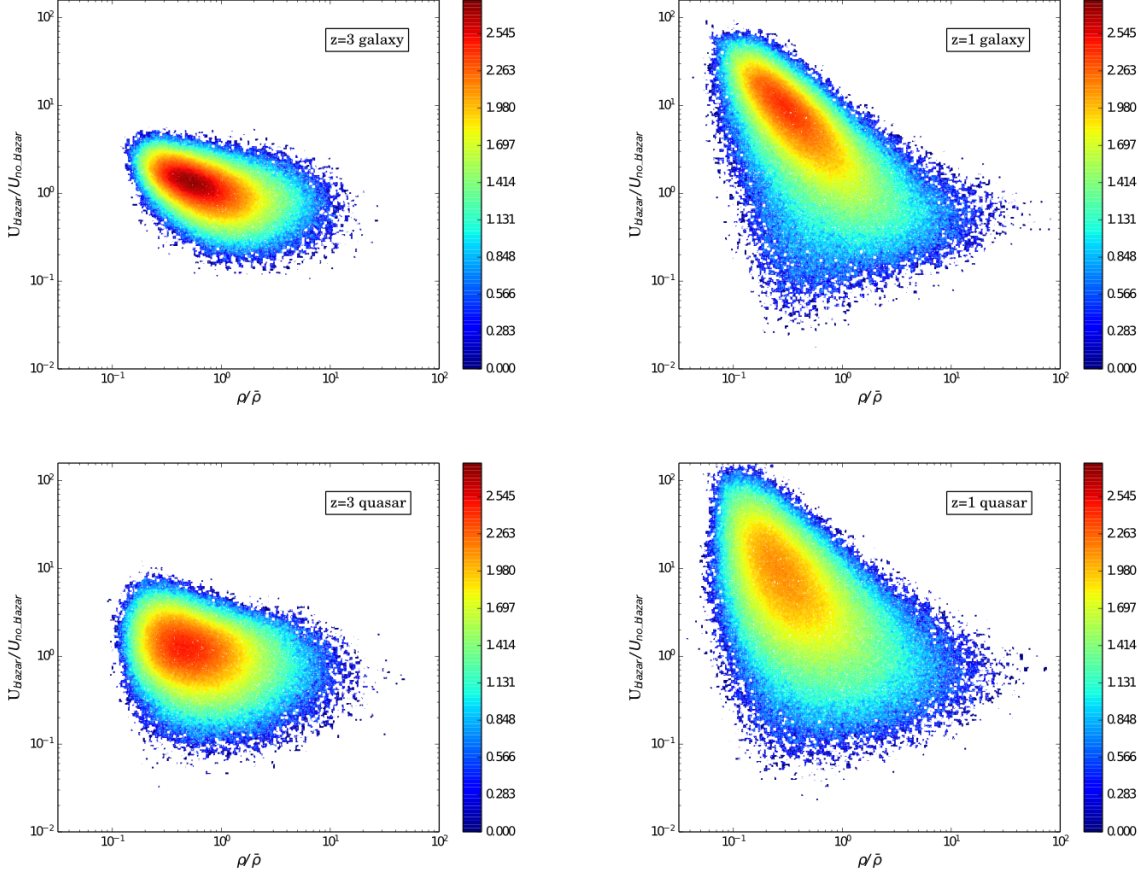


FIG. 3.— Ratio between the **internal energy when blazar heating is included and when it is not, as a function of overdensity. energy-injection due to blazar heating and the total internal energy**. The plots show the galaxy bias model (top) and the quasar bias model (bottom) for $z = 3$ (left) and $z = 1$ (right).

uniform case, translating the lower bias for galaxies.

5. DISCUSSION

Previous work on TeV blazar heating showed a significant increase in the temperature of the low density IGM (Chang et al. 2012; Puchwein et al. 2012). These results, while in good agreement with observational data for the mean transmitted flux statistics as well as fits to individual lines, appear to be in conflict with the recent work (Rudie et al. 2012). This observation suggest that a significant presence of gas in the IGM that has not been exposed to additional heating beyond photoheating. In the context of blazar heating, this suggests that the heating is not entirely uniform. In this work, we have studied the impact of inhomogeneous heating and find that when accounting for the clustering of sources, the variability in the heating rate is significant. In particular, we find that while most of the gas receives close to average heating, and has a temperature close to the uniform heating case, there is an important scatter in the temperature of the gas. If confirmed with the analysis of the resulting Lyman α forest, our model is able to account for both the observed increase in temperature in the low density IGM (Boera et al. 2014; Viel et al. 2009) and the lower values of the line widths as suggested by Rudie et al. (2012). The impact of inhomogeneous heating becomes especially important after $z = 2.5$. At such redshift, the impact of HeII reionization on the temperature of the

IGM is limited (Compostella et al. 2013). An increased temperature, with a strong scatter in underdense regions can then be attributed to inhomogeneous blazar heating. Such measurements are hard to obtain as the Lyman α forest is sensitive to overdensities of at least a few. The Lyman α forest of HeII traces lower density regions and is a promising observable, with more data becoming available (Worseck et al. 2014). A good understanding of the IGM is crucial as it is the birthplace of the large scale structures we observe. TeV blazar heating increases its average temperature and entropy, even at early times, and will impact the formation and evolution of structures (Pfrommer et al. 2012). Such heating occurs far away from the sources and is complimentary to other black hole feedback mechanisms directly impacting their host galaxies and clusters. Our model neglects important physical aspects of TeV blazars such as their duty cycle and beaming of the gamma-ray emission. The γ -ray duty cycle of BL Lac objects is of order of 10 % (Stecker & Salamon 1996). As TeV blazars have low accretion rates, their lifetime is long $\simeq 5 - 7$ Gyr (Cavaliere & D'Elia 2002). The γ ray sources are highly beamed, with observed opening angles peaking around 20° (Pushkarev et al. 2009). Parsec scale VLBI observations of the inner parts of radio jets indicate variations of the position angle of around 20° , up to 120° over more than a decade (Lister et al. 2013). [The following is slightly confusing;

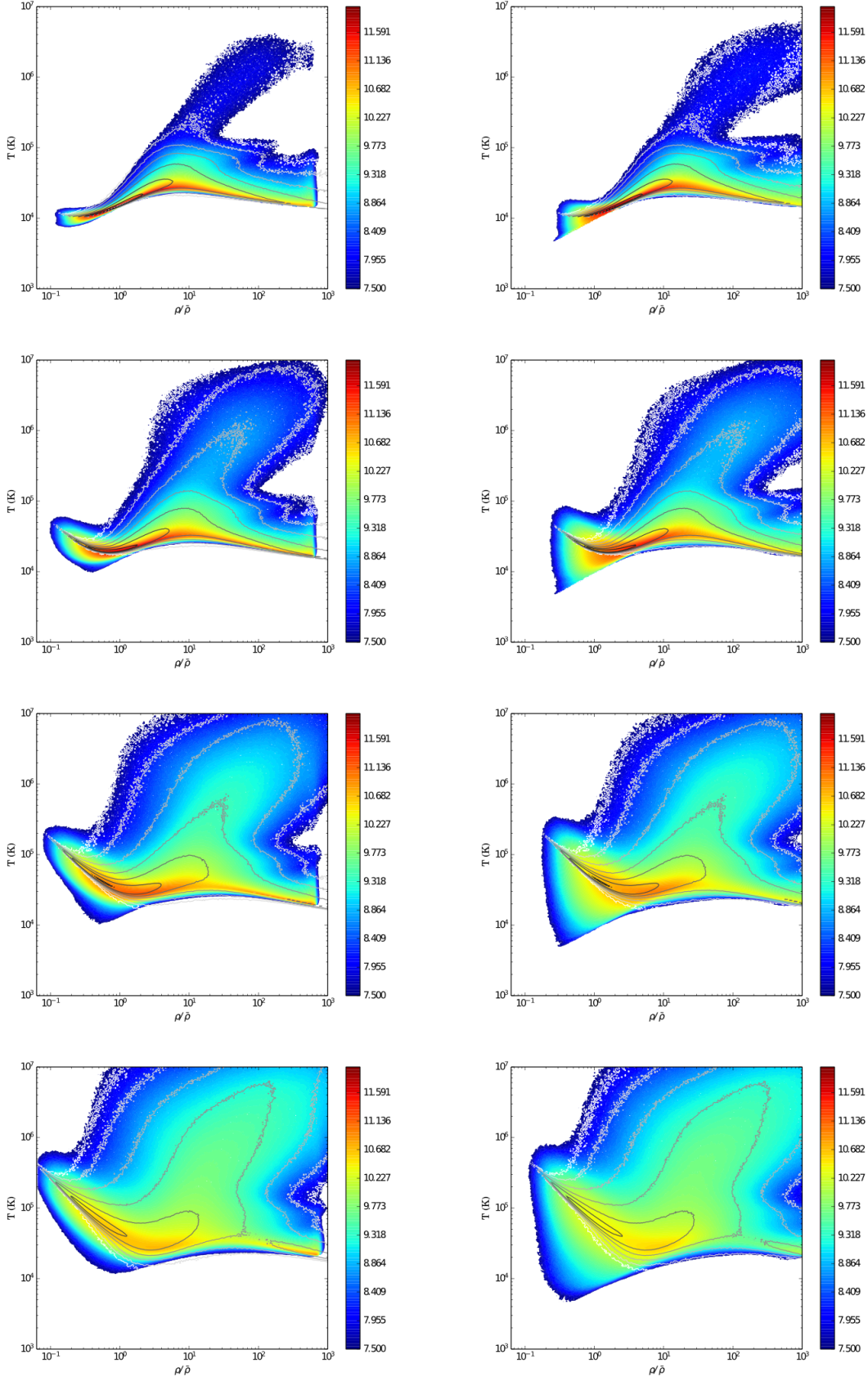


FIG. 4.— Mass weighted temperature - density relation at $z = 4, 3, 2, 1$ (from top to bottom) for the simulations with galaxy bias (left) and the quasar bias (right). The overlying grey contours show the corresponding $T - \rho$ relation for uniform blazar heating (Puchwein et al. 2012) for the same mass range.

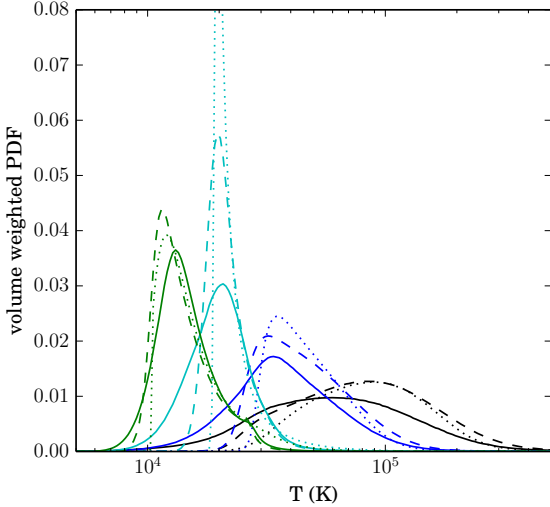


FIG. 5.— Volume-weighted temperature probability distribution function for $z = 1$ (black), 2 (blue), 3(cyan) and 4 (green) for the quasar bias model (solid line), galaxy bias model (dashed line) and the uniform case (dotted line).

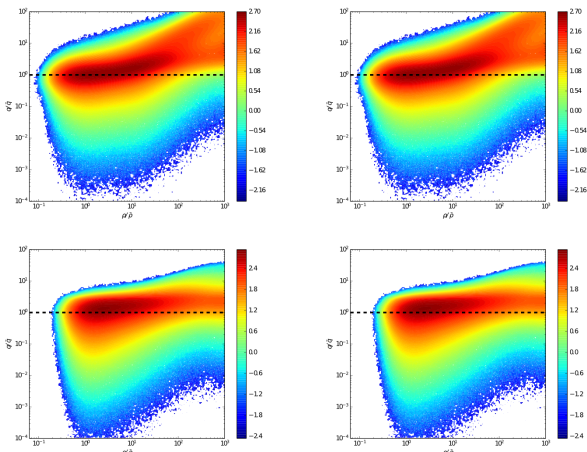


FIG. 6.— Volume-weighted distribution of heating rate fluctuations ($1+\delta_H$) with respect to the density fluctuations ($1+\delta$) for the galaxy bias model (upper row) and the quasar bias model (lower row) at $z = 3$ (left column) and $z = 1$ (right column). The black dashed line represents the case of uniform blazar heating.

a better stucture may help.] Both the beaming and small duty cycle yield additional variability in the distribution of the sources. If the number of sources of a given point is large, the variability of the heating rate will be reduced. However, when few sources are present, as in the early universe, individual variability increases the inhomogeneity of blazar heating. In such case, our model is a lower limit for the associated heating rate fluctuations. Similarly, our model does not take into account shot noise, which becomes important when sources are rare, such as in the early universe. This will result in additional heating rate fluctuations. Our model is based on quasar bias, which is likely lower than TeV-blazar bias (Allevato et al. 2014). Radio loud AGN are associated with red giant elliptical galaxies (Hyvönen et al. 2007) and are often at the center of small clusters and groups. Quasars have a wider distribution of host galaxies and

are rarely found at the center of clusters. Therefore, the scatter found in our simulations at low redshift is probably a lower limit to the exact scatter. In our simulations, any dense source emits TeV photons, regardless of the type of galaxy, and history of merger, accretion or star formation. However, a more detailed physical model, which comes at high computational cost, will likely give comparable results. The difference in the median temperature and standard deviation between the galaxy and quasar bias model is less than 5% which is smaller than current observational precision.

6. CONCLUSIONS

In this paper we have implemented inhomogeneous TeV blazar heating into cosmological simulations to study the impact of clustering on the thermal state of the intergalactic medium. This extends the work by Chang et al. (2012); Puchwein et al. (2012), based on uniform blazar heating. We developed a filtering function relating heating rate fluctuations to the linear dark matter fluctuations. Using this window function, we are able model the relevant length scales for the blazar heating fluctuations and include them in a statistical fashion. Our method is a cost effective alternative method to fully self consistent simulations of blazar heating where modeling black hole formation and growth and complete radiative transfer would have been prohibitive. Using this model for heating fluctuations, we find that large underdense regions receive less than one percent of the average heating rate while highly clustered regions receive up to five times more than the average heating rate at $z = 1$. Still, as in the uniform case, the impact of TeV blazar heating is the strongest in low density regions. In our simulations, the mode of the temperature of the IGM is very close to the value in the uniform model, indicating the uniform model is a good zeroth order approximation. However, the temperature density relations we obtain present a much larger scatter than the uniform case, especially at low redshift. In our quasar bias model, the temperature at mean density varies by an order of magnitude between the coldest and warmest regions. Our model for the blazar heating fluctuations yields a temperature density relation which can potentially reconcile the observed increased mean temperature of the IGM (Boera et al. 2014), while maintaining a fraction of cold gas, responsible for the lower envelope of the linewidth distribution (Rudie et al. 2012). Therefore, detailed modeling of the Lyman α forest will be the subject of a forthcoming paper. If confirmed, this will clearly indicate a more complex thermal history of the IGM, with potentially an important impact on late forming structures.

AL and PC is supported by the UWM Research Growth Initiative, the NASA ATP program through NASA grant NNX13AH43G, and NSF grant AST-1255469. A.E.B. and M.S. receive financial support from the Perimeter Institute for Theoretical Physics and the Natural Sciences and Engineering Research Council of Canada through a Discovery Grant. Research at Perimeter Institute is supported by the Government of Canada through Industry Canada and by the Province of Ontario through the Ministry of Research and Innovation. C.P. gratefully acknowledges financial support of the

Klaus Tschira Foundation. E.P. acknowledges support by the ERC grant “The Emergence of Structure during the epoch of Reionization”. The authors acknowledge the Texas Advanced Computing Center (TACC) at The University of Texas at Austin and the NASA Advanced

Supercomputing Division for providing HPC resources that have contributed to the research results reported within this paper.

APPENDIX

We detail the derivation of the window function of Eq. (4). We start from a purely Newtonian universe, then include the impact of expansion and finally various first order corrections to the received TeV flux.

NEWTONIAN CASE

Fluctuations with respect to the mean heating rate

The TeV flux received (in photons s⁻¹ cm⁻²) at position \mathbf{x} is given by the sum over all the sources within a radius $r \leq r_{\max}$.

$$J(\mathbf{x}) = \int_0^{2\pi} \int_0^\pi \int_0^{r_{\max}} \frac{\mathcal{E}(\mathbf{x}')}{4\pi|\mathbf{x}' - \mathbf{x}|^2} e^{-\tau} |\mathbf{x}' - \mathbf{x}|^2 \sin \theta d\theta d\phi d(\mathbf{x}' - \mathbf{x}), \quad (\text{A1})$$

where the emissivity \mathcal{E} is given in photons per unit time, per unit volume. $\tau = \kappa(\mathbf{x}' - \mathbf{x})$ is the optical depth along the line of sight, κ the absorption coefficient. Introducing $\mathbf{r}' = \mathbf{x}' - \mathbf{x}$, and $d\Omega = \sin \theta d\theta d\phi$ this gives

$$J(\mathbf{x}) = \int_\Omega \int_0^{r_{\max}} \frac{\mathcal{E}(\mathbf{r}' + \mathbf{x})}{4\pi} e^{-\tau} d\Omega dr'. \quad (\text{A2})$$

The corresponding heating rate (erg cm⁻³ s⁻¹) is given by

$$\dot{Q}(\mathbf{x}) = \frac{E_0}{D_{pp}} J(\mathbf{x}) = \frac{E}{4\pi} \int_\Omega d\Omega \int_0^{r_{\max}} \mathcal{E}(\mathbf{r}' + \mathbf{x}) \frac{1}{D_{pp}} e^{-\tau} dr', \quad (\text{A3})$$

with E_0 the mean energy of the TeV photons and D_{pp} their mean free path before they pair-produce. For convenience reasons, we do not take into account the integral on the spectral energy distribution of the TeV photons in this Appendix. This gives the heating rate per baryon

$$\dot{q}(\mathbf{x}) = \frac{\dot{Q}}{n} = \frac{E_0}{4\pi} \int_\Omega \int_0^{r_{\max}} \mathcal{E}(\mathbf{r}' + \mathbf{x}) \sigma e^{-\tau} d\Omega dr', \quad (\text{A4})$$

where n is the average density of the target photons (i.e. the EBL) and σ (in cm⁻²) is the energy averaged cross section for pair production on the extragalactic background light photons (Gould & Schréder 1967). The mean heating rate can be expressed as

$$\bar{q} = \frac{E_0}{4\pi} \int_\Omega d\Omega \int_0^{r_{\max}} \bar{\mathcal{E}} \sigma e^{-\tau} dr', \quad (\text{A5})$$

with $\bar{\mathcal{E}}$ the mean emissivity. Throughout the whole appendix, barred quantities are spatially averaged quantities. The heating rate fluctuations at a given point are then given by

$$\begin{aligned} \delta_H(\mathbf{x}) &= \frac{\dot{q}(\mathbf{x}) - \bar{q}}{\bar{q}} = \frac{E_0}{4\pi \bar{q}} \int_\Omega d\Omega \int_0^{r_{\max}} (\mathcal{E}(\mathbf{r}' + \mathbf{x}) - \bar{\mathcal{E}}) \sigma e^{-\tau} dr' \\ &= \frac{E_0}{4\pi \bar{q}} \int_\Omega d\Omega \int_0^{r_{\max}} \delta_E(\mathbf{r}' + \mathbf{x}) \bar{\mathcal{E}} \sigma e^{-\kappa r'} dr', \end{aligned} \quad (\text{A6})$$

with the fluctuations in the TeV emissivity δ_E such that one has $\delta_E = \delta$ if the emissivity fluctuations directly relate to the density fluctuations.

Window function

As the universe is infinite and asymptotically flat, we can expand the fluctuations into planar waves, in order to get the length scale dependence of heating rate fluctuations.

$$\begin{aligned} \delta_H(\mathbf{x}) &= \frac{1}{(2\pi)^3} \int_{-\infty}^{\infty} d^3 \mathbf{k}' \tilde{\delta}_H(\mathbf{k}') e^{-i\mathbf{k}' \cdot \mathbf{x}} \\ \delta_E(\mathbf{r}' + \mathbf{x}) &= \frac{1}{(2\pi)^3} \int d^3 \mathbf{k}' \tilde{\delta}_E(\mathbf{k}') e^{-i\mathbf{k}' \cdot (\mathbf{r}' + \mathbf{x})}, \end{aligned} \quad (\text{A7})$$

Eq. (A6) then gives

$$\frac{1}{(2\pi)^3} \int_{-\infty}^{\infty} d^3 \mathbf{k}' \tilde{\delta}_H(\mathbf{k}') e^{-i\mathbf{k}' \cdot \mathbf{x}} = \frac{E_0}{4\pi \bar{q}} \int_\Omega d\Omega \int_0^{r_{\max}} dr' \bar{\mathcal{E}} \sigma e^{-\kappa r'} \frac{1}{(2\pi)^3} \int d^3 \mathbf{k}' \tilde{\delta}_E(\mathbf{k}') e^{-i\mathbf{k}' \cdot (\mathbf{r}' + \mathbf{x})}. \quad (\text{A8})$$

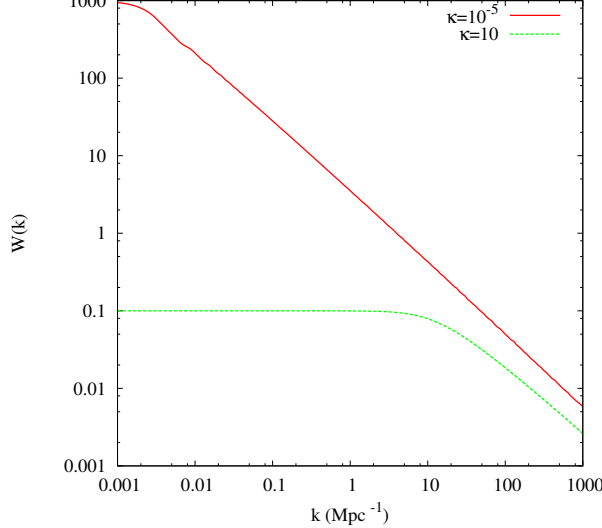


FIG. 7.— Window function for a non-expanding universe. The solid red line has very little absorption ($\kappa = 10^{-5} \text{ Mpc}^{-1}$), the dashed green line has $\kappa = 10 \text{ Mpc}^{-1}$.

Performing an inverse Fourier transform on the right-hand side of Eq. (A6), we have

$$\begin{aligned} &= \frac{1}{(2\pi)^3} \frac{E_0}{4\pi\bar{q}} \int_{\Omega} d\Omega \int_0^{r_{\max}} dr' \bar{\mathcal{E}} \sigma e^{-\kappa r'} \int d^3\mathbf{k}' \int d^3\mathbf{x} \tilde{\delta}_E(\mathbf{k}') e^{-i\mathbf{k}' \cdot \mathbf{r}'} e^{i(\mathbf{k}-\mathbf{k}') \cdot \mathbf{x}} \\ &= \frac{1}{(2\pi)^3} \frac{E_0}{4\pi\bar{q}} \int_{\Omega} d\Omega \int_0^{r_{\max}} dr' \bar{\mathcal{E}} \sigma e^{-\kappa r'} \int d^3\mathbf{k}' \delta^0(\mathbf{k} - \mathbf{k}') e^{-i\mathbf{k}' \cdot \mathbf{r}'} \tilde{\delta}_E(\mathbf{k}') \\ &= \frac{1}{(2\pi)^3} \frac{E_0}{4\pi\bar{q}} \int_{\Omega} d\Omega \int_0^{r_{\max}} dr' \bar{\mathcal{E}} \sigma e^{-\kappa r'} \tilde{\delta}_E(\mathbf{k}) e^{-i\mathbf{k} \cdot \mathbf{r}'}, \end{aligned} \quad (\text{A9})$$

with $\delta^{(0)}$ the Dirac function, which Fourier transform equals 1. Introducing $\mu = \cos\theta$, where θ is the angle between the wavevector and the line of sight, Eq. (A6) rewrites

$$\tilde{\delta}_H(\mathbf{k}) = \frac{E_0}{2\bar{q}} \int_{-1}^1 d\mu \int_0^{r_{\max}} \bar{\mathcal{E}} \sigma e^{-\kappa r'} \tilde{\delta}_E(k) e^{-ikr'\mu} dr' \quad (\text{A10})$$

$$\begin{aligned} &= \tilde{\delta}_E(\mathbf{k}) \frac{\sigma E_0}{\bar{q}} \int_0^{r_{\max}} \frac{\sin(kr')}{kr'} \bar{\mathcal{E}} e^{-\kappa r'} dr' \\ &= \tilde{\delta}_E(\mathbf{k}) \frac{\sigma E_0}{\bar{q}} \frac{\kappa}{k} \arctan\left(\frac{k}{\kappa}\right) \\ &= \tilde{\delta}(\mathbf{k}) \frac{\sigma E_0}{\bar{q}} \frac{\kappa}{k} \arctan\left(\frac{k}{\kappa}\right). \end{aligned} \quad (\text{A11})$$

Fig.7 shows window functions with different absorption coefficients in a purely Newtonian universe. The solid red line shows a case with no absorption, the dashed green line shows a case with $\kappa = 10 \text{ Mpc}^{-1}$. In the former case, large scale structure has the strongest impact on heating, as larger regions have more sources. When absorption is present, the impact of large scale structure (i.e. low k) remains constant as distant sources are absorbed. For scales equal to or larger than the cutoff, heating fluctuations follow density fluctuations and overdense regions get more heat. At smaller scales, the density structure has less impact on the heating, unless a strong overdensity is present.

EXPANDING UNIVERSE

We perform the same derivation as in the former section, replacing the integrals on the (comoving) distance by redshift integrals using

$$dr = \int \frac{c}{H(z)} dz'. \quad (\text{B1})$$

where $H(z)$ is the Hubble parameter.

$$\dot{q}(\mathbf{z}) = \frac{E_0(1+z)^2}{4\pi} \int_{\Omega} d\Omega \int_z^{z_{\max}} \frac{dl}{dz'} \sigma \mathcal{E}(E', z') e^{-\tau} dz'. \quad (\text{B2})$$

$z' = z + \Delta z$, with Δz the difference in redshift between the emission and reception of the photons. $\mathcal{E}(E', z')$ is the blazar luminosity at the energy E' , which then redshifts to energy E following [FIXED EQ. BELOW]

$$E' = E \frac{1+z'}{1+z}. \quad (\text{B3})$$

$\tau(E, z', z)$ is the optical depth of a TeV photon observed at redshift z with energy E , which was emitted at redshift z' with energy E' .

$$\tau(E, z', z) = \int_z^{z'} dz'' \frac{1}{D_{pp}} \frac{dl}{dz''} = \int_z^{z'} dz'' \frac{c}{H(z'')} \frac{1}{D_{pp}}, \quad (\text{B4})$$

Similarly to Eq. (A5), the mean heating rate is given by

$$\bar{\dot{q}} = \frac{E_0(1+z)^2}{4\pi} \int_{\Omega} d\Omega \int \frac{dl}{dz'} \sigma \bar{\mathcal{E}} e^{-\tau} dz'. \quad (\text{B5})$$

The resulting heating rate fluctuations are then given by

$$\begin{aligned} \delta_H(\mathbf{s}) &= \frac{\dot{q}(\mathbf{s}) - \bar{\dot{q}}}{\bar{\dot{q}}} = \frac{E_0(1+z)^2 c \sigma}{4\pi \bar{\dot{q}}} \int_{\Omega} d\Omega \int_z^{z_{\max}} \frac{(\mathcal{E}(z') - \bar{\mathcal{E}}) e^{-\tau}}{H(z')} dz' \\ &= \frac{E_0(1+z)^2 \bar{\mathcal{E}} c \sigma}{4\pi \bar{\dot{q}}} \int_{\Omega} d\Omega \int_0^{z_{\max}} \frac{\delta_E(z') e^{-\tau}}{H(z')} dz'. \end{aligned} \quad (\text{B6})$$

The TeV emission is related to the presence of supermassive black holes at the center of galaxies, which are located in collapsed dark matter halos. We can thus connect the fluctuations of the TeV emission, within a certain radius r , to the underlying dark matter fluctuations δ . At this stage we assume the TeV fluctuations exactly match the dark matter fluctuations $\delta_E = \delta$. We explain in the next section that this is not exactly true and will take into account various corrections. The initial density fluctuations represent a Gaussian random field, which exact properties depend on the earliest stages of the Universe prior to recombination (Bardeen et al. 1986; Peebles 1982). They grow linearly between z' and z following $\delta(z', r) = \delta_0(r) D(z')/D(z)$ (Heath 1977).

$$D(z) = D_0 H(z) \int_z^{\infty} \frac{1+z'}{H^3(z')} dz'. \quad (\text{B7})$$

The linear approximation breaks down when the amplitude of the root mean square of the perturbations approaches unity. The evolution of the density field is then determined by the spherical collapse (Gunn & Gott 1972) and the virialization of halos. As the growth of the modes is independent of the wavenumber, we have

$$\delta_E(z', r) = \delta(z', r) = \delta_o(r) D(z') = \delta_0 D(z') \frac{1}{(2\pi)^3} \int d^3 \mathbf{k}' \tilde{\delta}(\mathbf{k}') e^{-i\mathbf{k}' \cdot \mathbf{r}}. \quad (\text{B8})$$

And Eq. (B6) rewrites as

$$\delta_H(\mathbf{s}) = \frac{E_0(1+z)^2 \bar{\mathcal{E}} c \sigma}{4\pi \bar{\dot{q}}} \int_{\Omega} d\Omega \int_z^{z_{\max}} \frac{D(z')}{D(z)} \frac{\delta(r') e^{-\tau}}{H(z')} dz'. \quad (\text{B9})$$

The left hand side yields $\tilde{\delta}(\mathbf{k})$ while the right hand side transforms in a similar fashion to Eq. (A9). As the power spectrum of density fluctuations is isotropic, this yields

$$\tilde{\delta}_H(k) = \tilde{\delta}(k) \frac{E_0(1+z)^2 \bar{\mathcal{E}} c \sigma}{4\pi \bar{\dot{q}}} \int_z^{z_{\max}} \frac{D(z')}{D(z)} \frac{\sin(kr'(z'))}{kr'(z')} \frac{e^{-\kappa r'(z')}}{H(z')} dz'. \quad (\text{B10})$$

Fig. 8 shows the window function in an expanding universe at different redshifts. The TeV emission fluctuations are not exactly equal to the dark matter density fluctuations. In the next section we will account for the various corrections that have to be taken into account to determine a more accurate window function.

COMPLETE WINDOW FUNCTION

The TeV fluctuations are biased with respect to the dark matter fluctuations, as we detail in §2.2, yielding

$$\delta_E = (1 + b(z)\delta) \quad (\text{C1})$$

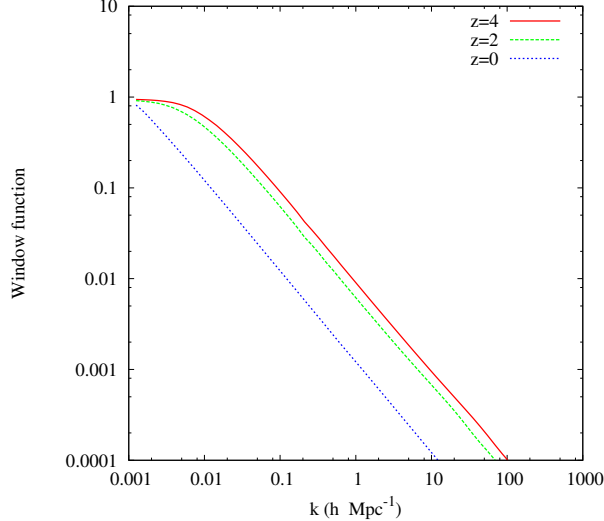


FIG. 8.— Window function in an expanding universe.

On top of that, the emitting area (which corresponds to the proper area), evolves as

$$4\pi r(z)^2 = 4\pi r^2 \left(\frac{\bar{\rho}}{\rho(z)} \right)^{2/3} = 4\pi r^2 (\delta(z) + 1)^{2/3}. \quad (\text{C2})$$

A small density perturbation thus gives

$$dA \simeq 4\pi \left(1 + \frac{2}{3}\delta \right) r^2. \quad (\text{C3})$$

If galaxies were moving exactly with the Hubble flow, their redshift would yield their exact distance to an observer. However, galaxies bound to the central potential of a cluster have an infall velocity towards the central overdensity. The proper distance to a source (Eq. (B1)) then becomes

$$dz' = dr \frac{H(z')}{c} \left(1 - \frac{d\delta_{v_r}(z')}{dr} \right), \quad (\text{C4})$$

where δ_{v_r} are the velocity perturbations along the line of sight. The Fourier transform of δ_{v_r} gives (Kaiser 1987).

$$\mathcal{F} \left(\frac{d\delta_{v_r}}{dr} \right) = -\mu^2 \tilde{\delta}(\mathbf{k}), \quad (\text{C5})$$

with μ the cosine of the angle between the wavenumber and the line of sight. Keeping only first order correction for density fluctuations, Eq. (B2) yields

$$\dot{q}(\mathbf{s}) = \frac{E_0(1+z)^2 c \sigma \bar{\mathcal{E}}}{4\pi} \int_{\Omega} d\Omega \int_z^{z_{\max}} \frac{D(z')}{D(z)} \left(1 + \left(b(z) + \frac{2}{3} \right) \delta(r) - \frac{d\delta_{v_r}}{dr} \right) dz'. \quad (\text{C6})$$

Subtracting the mean heating rate (Eq. (B5)) then yields the fluctuations

$$\delta_H(\mathbf{s}) = \frac{1}{X} \int_{\Omega} d\Omega \int_z^{z_{\max}} \frac{dX}{dz'} \frac{D(z')}{D(z)} \left(\left(b(z) + \frac{2}{3} \right) \delta(r) - \frac{d\delta_{v_r}}{dr} \right) dz', \quad (\text{C7})$$

where we introduced

$$\frac{dX}{dz'} = \frac{E_0(1+z)^2 \bar{\mathcal{E}} c \sigma}{4\pi} \frac{e^{-\tau(z, z', E')}}{H(z')}, \quad (\text{C8})$$

for convenience reasons and to highlight the generality of the method. Switching to k -space then yields

$$\begin{aligned}\tilde{\delta}_H(k) &= \frac{1}{X} \int_{\Omega} d\Omega \int_z^{z_{\max}} \frac{dX}{dz'} \frac{D(z')}{D(z)} \left(\left(b(z) + \frac{2}{3} \right) \delta(\mathbf{r}' + \mathbf{x}) - \frac{d\delta_{vr}(\mathbf{r}' + \mathbf{x})}{dr} \right) dz' \\ &= \frac{1}{X} \int_{\Omega} d\Omega \int_z^{z_{\max}} \frac{dX}{dz'} \frac{D(z')}{D(z)} \left(\left(b(z) + \frac{2}{3} \right) \int d^3 \tilde{\delta}(\mathbf{k}') \delta^{(0)}(\mathbf{k} - \mathbf{k}') e^{-i\mathbf{k}' \cdot \mathbf{r}'} \tilde{\delta}(\mathbf{k}') - \int d^3 \mathbf{k}' e^{-i\mathbf{k}' \cdot \mathbf{r}'} \delta(\mathbf{k}') \delta^{(0)}(\mathbf{k} + \mathbf{k}') \mu^2 \right) dz' \\ &= \frac{\tilde{\delta}(\mathbf{k})}{X} \int_{-1}^1 d\mu \int_z^{z_{\max}} \frac{dX}{dz'} \frac{D(z')}{D(z)} \left(\left(b(z) + \frac{2}{3} \right) + \mu^2 \right) e^{-ikr\mu} dz' \\ &= \frac{\tilde{\delta}(\mathbf{k})}{X} \int_z^{z_{\max}} \frac{dX}{dz'} \frac{D(z')}{D(z)} \left((b(z) + 1) j_0(kr) - \frac{2}{3} j_2(kr) \right) dz'.\end{aligned}\quad (\text{C9})$$

With the spherical Bessel functions

$$j_0(kr) = \frac{\sin(kr)}{kr} \quad (\text{C10})$$

$$j_2(kr) = \left(\frac{3}{x^2} - 1 \right) \frac{\sin(x)}{x} - \frac{3\cos(x)}{x^2}. \quad (\text{C11})$$

We have used

$$\int_{-1}^1 \mu^2 e^{ikr\mu} d\mu = \frac{2\sin(kr)}{kr} + 4 \frac{\cos(kr)}{(kr)^2} - 4 \frac{\sin(kr)}{(kr)^3}. \quad (\text{C12})$$

The window function for the heating rate fluctuations is then given by

$$\tilde{W}_H(k, z) = \frac{E_0(1+z)^2 \sigma c \bar{\mathcal{E}}}{4\pi \bar{q}} \int_z^{z_{\max}} \frac{e^{-\tau}}{H(z')} \frac{D(z')}{D(z)} \left((b(z) + 1) j_0(kr) - \frac{2}{3} j_2(kr) \right) dz'. \quad (\text{C13})$$

Which is the same window function as Pritchard & Furlanetto (2007); Barkana & Loeb (2005).

REFERENCES

- Aleksić, J., Antonelli, L. A., Antoranz, P., et al. 2010, A&A, 524, A77
 Allevato, V., Finoguenov, A., & Cappelluti, N. 2014, arXiv:1410.0358
 Bardeen, J. M., Bond, J. R., Kaiser, N., & Szalay, A. S. 1986, ApJ, 304, 15
 Barkana, R., & Loeb, A. 2005, ApJ, 626, 1
 Basilakos, S., Plionis, M., & Ragone-Figueroa, C. 2008, ApJ, 678, 627
 Boera, E., Murphy, M. T., Becker, G. D., & Bolton, J. S. 2014, MNRAS, 441, 1916
 Bolton, J. S., & Becker, G. D. 2009, MNRAS, 398, L26
 Bolton, J. S., Becker, G. D., Haehnelt, M. G., & Viel, M. 2014, MNRAS, 438, 2499
 Bolton, J. S., Viel, M., Kim, T.-S., Haehnelt, M. G., & Carswell, R. F. 2008, MNRAS, 386, 1131
 Bond, J. R., Kofman, L., & Pogosyan, D. 1996, Nature, 380, 603
 Bret, A., Firpo, M.-C., & Deutsch, C. 2004, Phys. Rev. E, 70, 046401
 Broderick, A. E., Chang, P., & Pfrommer, C. 2012, ApJ, 752, 22
 Broderick, A. E., Pfrommer, C., Puchwein, E., & Chang, P. 2013, ApJ, in print, arXiv:1308.0015
 —. 2014, ApJ, 790, 137
 Cavalieri, A., & D'Elia, V. 2002, ApJ, 571, 226
 Chang, P., Broderick, A. E., & Pfrommer, C. 2012, ApJ, 752, 23
 Chang, P., Broderick, A. E., Pfrommer, C., et al. 2015, ApJL submitted
 Clowes, R. G., Harris, K. A., Raghunathan, S., et al. 2013, MNRAS, 429, 2910
 Compostella, M., Cantalupo, S., & Porciani, C. 2013, MNRAS, 435, 3169
 Cooray, A., & Sheth, R. 2002, Phys. Rep., 372, 1
 Croom, S. M., Boyle, B. J., Shanks, T., et al. 2005, MNRAS, 356, 415
 Dermer, C. D., Cavadi, M., Razzaque, S., et al. 2011, ApJ, 733, L21
 Durrer, R., & Neronov, A. 2013, A&A Rev., 21, 62
 Faucher-Giguère, C.-A., Lidz, A., Zaldarriaga, M., & Hernquist, L. 2009, ApJ, 703, 1416
 Franceschini, A., Rodighiero, G., & Vaccari, M. 2008, A&A, 487, 837
 Giommi, P., Padovani, P., & Polenta, G. 2013, MNRAS, 431, 1914
 Giommi, P., Padovani, P., Polenta, G., et al. 2012, MNRAS, 420, 2899
 Gould, R. J., & Schréder, G. P. 1967, Physical Review, 155, 1408
 Gunn, J. E., & Gott, III, J. R. 1972, ApJ, 176, 1
 H. E. S. S. Collaboration, Abramowski, A., Aharonian, F., et al. 2014, A&A, 562, A145
 Heaton, D. J. 1977, MNRAS, 179, 351
 Hockney, R. W., & Eastwood, J. W. 1981, Computer Simulation Using Particles
 Hopkins, P. F., Richards, G. T., & Hernquist, L. 2007, ApJ, 654, 731
 Hyvönen, T., Kotilainen, J. K., Falomo, R., Örndahl, E., & Purisimo, T. 2007, A&A, 476, 723
 Kaiser, N. 1987, MNRAS, 227, 1
 Kneiske, T. M., Bretz, T., Mannheim, K., & Hartmann, D. H. 2004, A&A, 413, 807
 Komatsu, E., Smith, K. M., Dunkley, J., et al. 2011, ApJS, 192, 18
 Kravtsov, A. 2010, Advances in Astronomy, 2010, arXiv:0906.3295
 Lister, M. L., Aller, M. F., Aller, H. D., et al. 2013, AJ, 146, 120
 Mandelbaum, R., Li, C., Kauffmann, G., & White, S. D. M. 2009, MNRAS, 393, 377
 McQuinn, M., Lidz, A., Zaldarriaga, M., et al. 2009, ApJ, 694, 842
 Miniati, F., & Elyiv, A. 2013, ApJ, 770, 54
 Mo, H. J., & White, S. D. M. 1996, MNRAS, 282, 347
 Myers, A. D., Brunner, R. J., Nichol, R. C., et al. 2007, ApJ, 658, 85
 Neronov, A., & Semikoz, D. V. 2009, Phys. Rev. D, 80, 123012
 Peebles, P. 1982, Principles of Physical Cosmology, ed. T. Anderson, Wightman (Princeton University Press)
 Pfrommer, C., Chang, P., & Broderick, A. E. 2012, ApJ, 752, 24
 Pontzen, A. 2014, Phys. Rev. D, 89, 083010

- Pritchard, J. R., & Furlanetto, S. R. 2007, MNRAS, 376, 1680
 Puchwein, E., Bolton, J. S., Haehnelt, M. G., Madau, P., &
 Becker, G. D. 2014, ArXiv e-prints, arXiv:1410.1531
 Puchwein, E., Pfrommer, C., Springel, V., Broderick, A. E., &
 Chang, P. 2012, MNRAS, 423, 149
 Pushkarev, A. B., Kovalev, Y. Y., Lister, M. L., & Savolainen, T.
 2009, A&A, 507, L33
 Rauch, M., Miralda-Escude, J., Sargent, W. L. W., et al. 1997,
 ApJ, 489, 7
 Regan, J. A., Haehnelt, M. G., & Viel, M. 2007, MNRAS, 374,
 196
 Ricotti, M., Gnedin, N. Y., & Shull, J. M. 2000, ApJ, 534, 41
 Rudie, G. C., Steidel, C. C., & Pettini, M. 2012, ApJ, 757, L30
 Schaye, J., Theuns, T., Rauch, M., Efstatithiou, G., & Sargent,
 W. L. W. 2000, MNRAS, 318, 817
 Schlickeiser, R., Ibscher, D., & Supsar, M. 2012, ApJ, 758, 102
 Schlickeiser, R., Krakau, S., & Supsar, M. 2013, ApJ, 777, 49
 Shen, Y., Strauss, M. A., Oguri, M., et al. 2007, AJ, 133, 2222
 Simionescu, A., Werner, N., Böhringer, H., et al. 2009, A&A, 493,
 409
 Simpson, C., Rawlings, S., Ivison, R., et al. 2012, MNRAS, 421,
 3060
 Sironi, L., & Giannios, D. 2014, ApJ, 787, 49
 Springel, V. 2005, MNRAS, 364, 1105
 Springel, V., & Hernquist, L. 2002, MNRAS, 333, 649
 Stecker, F. W., de Jager, O. C., & Salamon, M. H. 1992, ApJ,
 390, L49
 Stecker, F. W., Malkan, M. A., & Scully, S. T. 2006, ApJ, 648,
 774
 Stecker, F. W., & Salamon, M. H. 1996, ApJ, 464, 600
 Viel, M., Bolton, J. S., & Haehnelt, M. G. 2009, MNRAS, 399,
 L39
 Viel, M., Haehnelt, M. G., & Springel, V. 2004, MNRAS, 354, 684
 Vovk, I., Taylor, A. M., Semikoz, D., & Neronov, A. 2012, ApJ,
 747, L14
 Werner, N., Simionescu, A., Million, E. T., et al. 2010, MNRAS,
 407, 2063
 Worseck, G., Prochaska, J. X., Hennawi, J. F., & McQuinn, M.
 2014, ArXiv e-prints, arXiv:1405.7405